Influence of the porosity pattern on the aerodynamics of a square-shaped fly-swatter

Ariane Gayout, M. Bourgoin, Nicolas Plihon

Influence of the porosity pattern on the aerodynamics of a square-shaped fly-swatter

A. Gayout,[1, a)] M. Bourgoin,[1] and N. Plihon[1]
Univ Lyon, ENS de Lyon, CNRS, Laboratoire de Physique, F-69342 Lyon, France

(*Electronic mail: a.m.m.gayout@rug.nl)

(Dated: 8 January 2024)

The evolution of the normal aerodynamic coefficient of 19 configurations of square plates with various porosity patterns, ranging from solid plate to homogeneous porous plate, is experimentally characterized. The variation of the porosity pattern is obtained by partially covering the holes of a commercial fly-swatter using adhesive tape. Evolution of the normal aerodynamic coefficient is assessed from the measurement of the angular position of the porous plate, placed as a freely rotating pendulum swept by a flow in a wind tunnel. These angular measurements are also supported by Particle Image Velocimetry measurements of the structure of the wake. We show that the porosity pattern determines whether or not an abrupt stall occurs. In particular, the details of the porosity pattern on the edges of the plate are decisive for the existence of abrupt stall.

I. INTRODUCTION

The omnipresence of porous structures in Nature and in technological applications induces complexity in a wide range of physical problems. In the context of technological applications, the water flow through nets and the drag exerted on net structures is crucial for aquaculture[1]. The use of porous structures and fences has long been proposed as a means of controlling the characteristics of flows, with a number of important applications in aerodynamics or civil engineering[2,3]. The development of fog harvesters for water supply in arid regions requires a fine understanding of flows in the vicinity of nets[4,5]. At smaller scales, the efficiency of respiratory masks to reduce the propagation of airborn viruses rely on reducing the amount and distance of aerosols spread following the propagation of multiphase flows through finely meshed masks[6,7]. Porous disks have also recently been widely used as simple and effective models for wind turbine actuation disks, which accurately reproduce the transport of kinetic energy in the far wake of the wind turbine, where rotation can be neglected[8–11]. Most of the research on porous disks has been carried out in the context of onshore wind turbines and fixed horizontal-axis wind turbines, with normal-incidence flows on the porous disk, although recent interest has also been seen in vertical-axis wind turbines[12]. The development of floating offshore wind turbines now raises the issue of modeling wind interaction with porous discs at various incidence angles, as the turbine oscillates back and forth due to the interaction of the floating structure with water waves[13–16] In the context of wind-dispersed plant seed, the flight of the dandelion involves a porous structure made of a bundle of bristles. It was recently demonstrated that the aerodynamic drag was maximized thanks to a specific structure of the wake, namely a separated of a vortex ring[17,18]. Bristled wing are also widespread in Nature and were shown to increase lift at small Reynolds numbers[19,20].

Fundamental aerodynamics studies of porous materials date back to the pioneering work of G.I. Taylor[21,22], and largely focused on the influence of porosity on pressure drop and on drag at normal incidence. Castro investigated the influence of the porosity fraction of perforated plates with centimetric-holes and showed a drag decrease as the porosity fraction increases and the absence of vortex shedding for porous fractions above ~ 0.2[23]. These early works have then been refined by Graham[24] and Roberts[25]. Several experimental studies then focused, for instance, on the interaction

[a)]Also at Biomimetic Group, Energy and Sustainability Research Institute Groningen, Faculty of Science and Engineering, University of Groningen, 9747 AG Groningen, The Netherlands

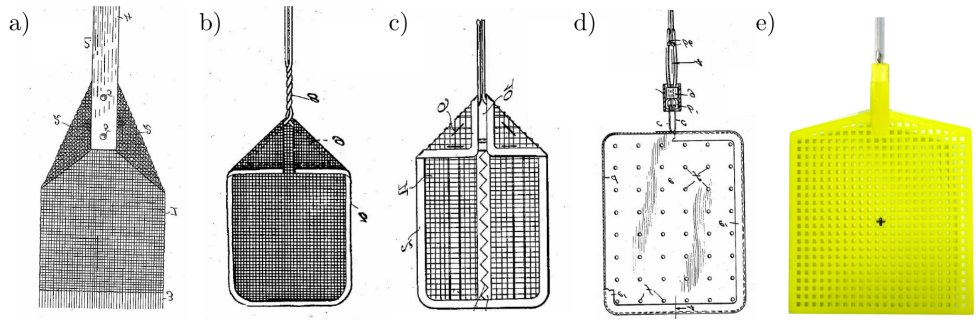

FIG. 1. a) Fly-killer in 1900 from[34]. b) Fly-swatter in 1927 from[35]. c) Fly-swatter in 1938 from[36]. d) Fly-swatter in 1939 from[37]. e) Fly-swatter used in this article .

of periodically arranged jets emerging from porous screens[26] or the shape of the perforated obstacle[27]. The modelling of the flow behind porous screen at normal incidence also attracted attention since the work of Taylor[21] who considered a porous screen as a uniform distribution of sources. Koo & James then refined this model for a two-dimensional porous screen confined within a channel[28], and extended by Steiros & Hultmark to include a base-suction term to improves the predictions at low porosities[29]. Very recently, an extension to three-dimensional flows, taking into account the porous screen shape and viscous effects, has been proposed[30].

Note that all these studies were done for homogeneous porosity pattern. De Bray studied experimentally the influence of the porosity pattern on the drag coefficient of a perforated square plate for which successive rows of holes were blocked concentrically inwards or outwards, at normal incidence[31]. The drag coefficient increases as the porous fraction decreases (defined as the ratio between the open surface and the gross area of the plate, and called the free surface ratio by De Bray). Interestingly, for a given porosity fraction, the drag coefficient increases more rapidly when the outer rows are covered than when the inner rows are covered, and similar trends will be described at various incidence angle in Sec. III B. Surprisingly, the effect of the angle of attack on the aerodynamic coefficients and the flow features of porous screen has only recently been studied experimentally and theoretically[30], though it was shown that porosity strongly influences the trajectory of permeable or porous disks[32], or its stability[33]. In this article, we extend these previous work and study experimentally the aerodynamic coefficients of porous plates with inhomogeneous porosity pattern, and span a wide range of angles of attack. Our strategy was to systematically vary the porosity pattern by partially covering a porous plate with a large numbers of holes, and we chose an ideal object widely spread for this study: a fly-swatter.

Fly-swatters are indeed typically constructed using porous media, since the first modern model in 1900, the “Fly-Killer”, which was composed of a rectangular wired net[34]. The use of wire-netting was introduced for durability and elasticity but no reference on the aerodynamic advantage of such netting is mentioned in this initial patent. Later improvements mostly concerned the handle to ease the motion of the fly-swatter[35,36]. Even when a different kind of fly-swatter, made of a rubber surface with a few holes, was introduced in 1939[37], no aerodynamic considerations are presented and it seems that holes were added empirically, to either reduce costs or increase elasticity. Sketches of the above-mentioned fly-swatter are reproduced in Fig. 1.a-d), together with a photograph of the modern plastic model used for the present investigation, whose porous fraction is 28% when all holes are opened. In this article, we investigate how the porous pattern, modified by covering some holes of the fly-swatter, influence the aerodynamic coefficients and might be an important factor to optimize the aerodynamics of fly-swatters

The evolution of the normal aerodynamic coefficient (see next section) when varying the angle of attack the porosity was obtained placing the fly-swatter at the bottom of a freely rotating rod, acting as a pendulum, and placed in a wind tunnel, following a setting previous investigated[38,39]. As the wind speed increases, the angular position evolves and is set by the torque balance[38,39]. When an abrupt stall occurs, the result is a discontinuity in angular position between a drag-dominated

branch and a lift-dominated branch, possibly leading to bistability[38,39]. The transitions between the two branches were shown to be controlled by rare aerodynamics events[39], making this aerodynamic pendulum one of the simplest experimental configuration to study rare-event statistics.

This article is organized as follows: Sec. II describes the experimental setup, and how the evolution of the normal aerodynamic coefficient with the inclination angle is extracted for the evolution of the inclination angle with the flow velocity. The results are then presented and discussed in Sec. III, with a focus on the differences between a solid and a porous plate in Sec. III A, and the investigation of 19 different porosity patterns, where the holes of the fly-swatter were covered concentrically in Sec. III B and with a focus on the influence of the porosity of the edges of the fly-swatter in Sec. III C. Conclusions are then drawn in Sec. IV.

II. EXPERIMENTAL SETUP

The influence of the porosity pattern on the aerodynamic coefficients has been experimentally evaluated using the plastic fly-swatter shown in Fig. 1.e). The fly-swatter consists in a 1.5 mm thick plastic square of size $a = 10\,\text{cm}$ with square holes of size 2.4 mm equally spaced at a distance of 1.8 mm. Each row and column of the square section contains 22 holes, for a total of 484 holes. A small triangular shape at the top of the fly-swatter, with 26 holes on each side, connects the square section to the fly-swatter holder. For all the configurations detailed in this article, the holes of this small triangular shape are left open.

In this article, we will focus on the influence of the porosity pattern of the square section on the aerodynamic coefficients of the system, and the holes of the upper triangular part will be left open. The porosity pattern is modified by adding adhesive vinyl tape to block specific holes (see Sec. III B for details). The vinyl tape was placed so that only rows or columns of 2-hole width were sealed by one piece of tape, and no tape peeling was observed over the various experiments. The maximum porous fraction, given as the ratio between the surface of the 484 holes and the surface of the whole square is 28%. Of the 2^{484} possible configurations for the partial covering of the fly-swatter, we decided to select only 19 with left-right symmetry and to focus on the onset of stall when the porosity pattern is modified. For 11 of them, due to a slight curvature of the fly-swatter, two sets of measurements were carried out, one with the curvature facing upstream and the other downstream, as will be discussed in Sec. III D.

The aerodynamic coefficients of the plates with various porosity patterns are assessed from measurements in a wind tunnel, as sketched in Fig. 2, following the protocol detailed elsewhere[39,40], and recalled here. The wind tunnel is closed-loop and has a closed section, a 51 cm width square, with a flow conditioned through a honeycomb leading to a typical ambient turbulence rate of 2%. The wind velocity spans between 1 and $7\,\text{m}\,\text{s}^{-1}$, resulting in Reynolds numbers, based on the fly-swatter a, ranging between 6×10^3 and 5×10^4. The fly-swatter, placed facing the flow, is attached at the extremity of a rod free to rotate around point O. The rod consists of a 1 cm-thick, 1 mm-wide aluminium rigid plate covered by a 3 mm-wide plastic streamlined profile. The overall contribution of the rod to the aerodynamic forces can be neglected for three reasons. Firstly, the frontal surface of the rod is more than an order of magnitude smaller than that of the fly-swatter. Secondly, a rough estimate of the aerodynamic forces on the empty rod at maximum velocity gives about 4 to 5% of the total forces on the fly-swatter, at the same velocity. Lastly, as the rod design is kept constant over the whole experiment, we consider that the possible effects of the rod are constant over the whole range of parameters we explore and should thus not influence the relative comparison between configurations presented below.

The flexibility of the fly-swatter was not precisely determined, however, no deformation of the fly swatter was observed, even at the highest flow velocity, showing that flexibility of the system can be ignored for our investigation. It is also firmly established that the sharpness of the corners in the streamwise direction (i.e. for the thickness of the fly-swatter) has a significant influence on the flow field[41]. For the fly-swatter used in this study, both the edges and the holes are sharp (i.e., in Fig 1.e, the radius of curvature of the edges is negligible in the transverse direction). The corners of the square have a 2.5 mm radius of curvature.

Frictionless rotation of this pendulum is obtained using an air bushing (OAVTB16i04 from OAV

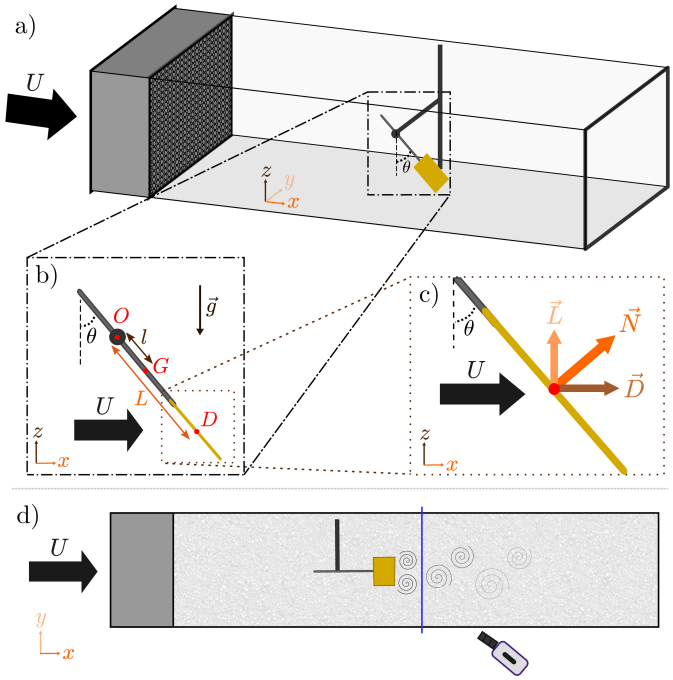

FIG. 2. a) Schematic view of the wind tunnel with the fly-swatter. b) Details of the pendular attachment of the fly-swatter. c) Definition of the aerodynamic forces. d) PIV setup overview.

Labs), and the angular position θ with respect to the vertical is recorded by a contact-less rotary encoder with minimal friction (DS- 25, 17-bit digital encoder from Netzer). Note that the angle θ is complementary to the angle of attack, as usually defined in aerodynamic studies. The distance between the pivot point O and the center of the fly-swatter is $L = 17.3\,\text{cm}$. The distance l between point O and center of mass G of the pendulum is computed for each configuration, knowing the mass of the rod and of the fly-swatter and measuring the mass of the added vinyl tape strips. The pivot point O is located at $z = 33.5$ cm, and the pendulum oscillates in the midplane of the wind tunnel. The minimal distance between the fly swatter and the walls of the wind tunnel is thus 10 cm. The flow impinging the porous square exerts an aerodynamic torque Γ_{aero} at point O, due to both lift and drag, and the equation of motion reads $J\ddot{\theta} = -mgl\sin\theta + \Gamma_{\text{aero}}$, with J the moment of inertia of the pendulum. The aerodynamic forces acting on the fly-swatter (see Fig. 2c) are the drag force $\mathbf{D} = \frac{1}{2}\rho L U^2 a^2 C_D(\theta)\mathbf{e_x}$ and the lift force $\mathbf{L} = \frac{1}{2}\rho L U^2 a^2 C_L(\theta)\mathbf{e_z}$, with ρ the air density, a the side of the square plate and where the drag coefficient C_D and the lift coefficient C_L depend on θ[42]. The total aerodynamic torque is expressed as $\frac{1}{2}\rho L U^2 a^2 C_N(\theta)$, where the normal coefficient C_N is defined as $C_D\cos\theta + C_L\sin\theta$[38]. In this article, we will focus on steady state regimes, for which the torque induced by the weight of the pendulum balances the aerodynamic torque:

$$mgl\sin(\theta) = \frac{1}{2}\rho U^2 a^2 L C_N(\theta) \tag{1}$$

We made the choice of ignoring the covering fraction for the area a^2 of the fly-swatter used to define the aerodynamic coefficients, as we expect it to not be a simple proportionality factor due to the aerodynamic coupling of holes in the array. This choice was further confirmed by DeBray's previous study[31]. As mentioned above, the mass m has been measured for each configuration, due to the vinyl tape adding up to 2 g to the fly-swatter when fully covered, and l was computed accordingly. For each configuration, the mean angle θ is measured over at least 15 s for each flow velocity, ensuring statistical convergence of the mean-value, and the normal aerodynamic coefficient $C_N(\theta)$ is computed from Eq. 1.

In addition to the recording of the angular position, Particle Image Velocimetry (PIV) has been

implemented in the wind tunnel to enable flow visualization in the wake of the fixed fly-swatter. This flow visualization is done in the transverse (y,z) plane. This choice was in particular motivated by the tri-dimensionality of the wake for pendulums of aspect ratio close to 1[43]. The flow structure is obtained from smoke particle imaging. Particles are illuminated from a laser sheet produced by a 5 W blue diode laser through a Powell lens with a 30° fan angle, and imaged using a high-speed camera (Phantom v26.40) at a resolution of 2048 by 1952 pixels and a 100 mm lens through a Scheimpflug adaptor to ensure focus on a transverse plane inside the wind tunnel. As we chose to visualize the transverse (v,w) flow in the (y,z) plane , the particles only remain in the sheet for a short time, which imposes constraints on the flow velocity (set to $1.7\,\mathrm{m\,s^{-1}}$), the thickness of the laser sheet (4 mm was observed to be an optimal choice) and the frame rate (set to 2000 fps). The PIV algorithm uses the open software UVMAT[44].

III. RESULTS

A. Solid versus homogeneous porous square

Let us first focus on the main differences between a solid square (i.e. all holes have been covered by vinyl tape) and a homogeneous porous square (i.e. the original fly-swatter geometry), before investigating more complex patterns in the following subsections.

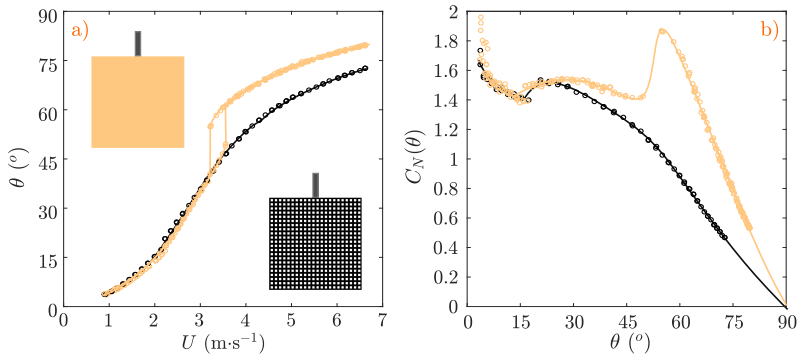

FIG. 3. Aerodynamic response of the fly-swatter (black) compared to a square plate (beige): a) evolution of θ as a function of U, b) C_N coefficient computed from a) and Eq. 1. The curves are spline interpolations and thus an eye guide. Data points are available as Supplementary Material.

Figure 3.a) shows the evolution of the angular position θ as a function of the wind velocity U for the solid square (orange) an the porous square (black). The evolution of the normal aerodynamic coefficient $C_N(\theta)$ as a function of θ, computed from Eq. 1, is shown in Fig. 3.b). We note that $\theta(U)$ exhibits abrupt transitions and bistability for the solid plate, which can be readily understood from the evolution of the steady-state aerodynamic coefficients (see detailed discussions in Ref.[38,39]). For velocities below the bistable region (and angles below 50°), the dominant aerodynamic force is the drag force, and corresponds to a nearly constant C_N value. For velocities above the bistable region (and angles above 53°), the dominant aerodynamic force is the lift force. The stall angle corresponds to a dramatic decrease of C_N with decreasing angle, namely at around 52° for the solid square, and translates in abrupt transition in the evolution of θ as a function of U. We stress that this stall angle is in agreement with values observed for flat square by Eiffel ($\theta_{stall} \simeq 51°$)[45], Flachsbart ($\theta_{stall} \simeq 50°$)[42] and more recently by Okamoto and Azuma ($\theta_{stall} \simeq 50°$ - note that θ is complementary to the angle of attack)[46]. Remarkably, the transition is smoother for the homogeneous porous square, and there is no abrupt stall angle. We note two noteworthy features at low angles, for both configurations. The first one is a strong increase of C_N as θ is decreased below a 10 degrees, and is discussed further in Sec. III D. The second one is the bump observed on C_N between 15° and 18°, which is attributed to the presence of stall on the holding rod. In the remaining of this article (apart from Sec. III D), we will thus ignore the evolution of the C_N coefficient below 18°, and we will focus on the conditions

for which an abrupt stall is observed when varying the porosity pattern (data below 18° will be systematically shown as lighter symbols in the remaining of this article).

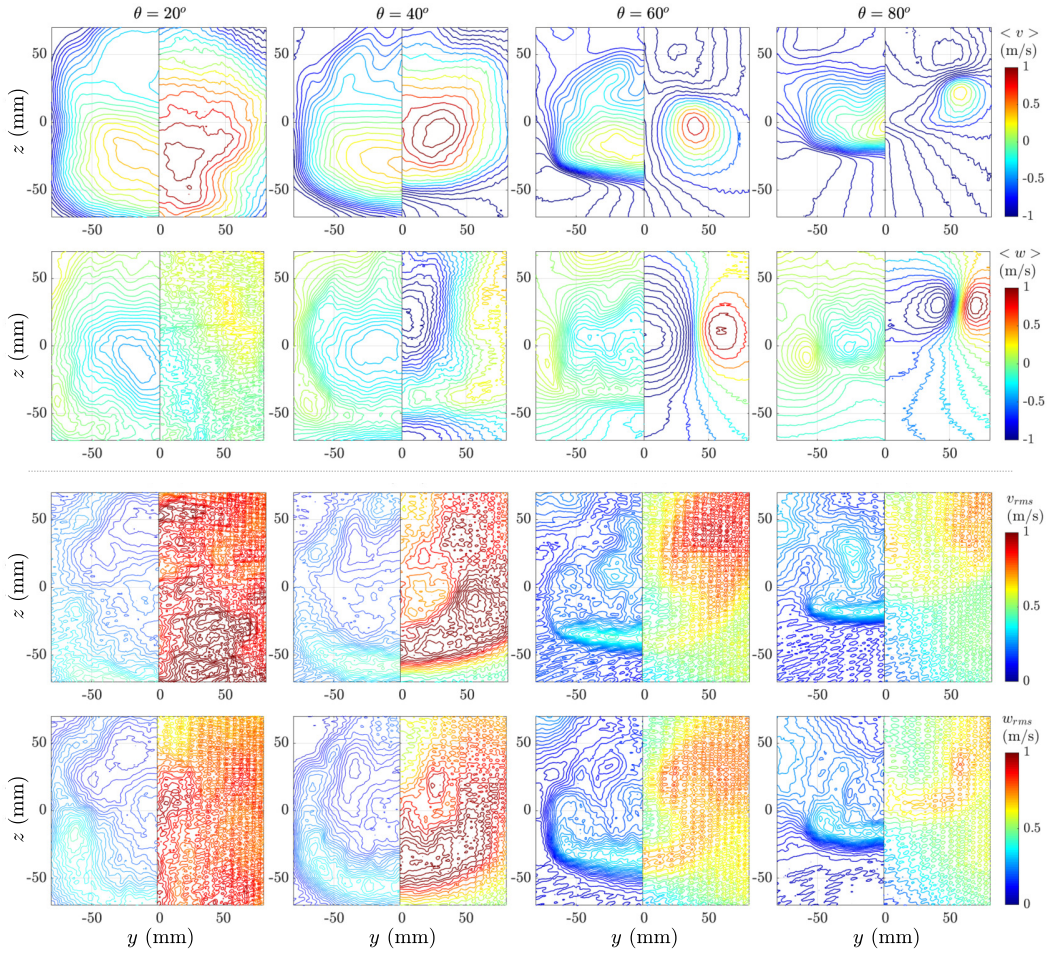

FIG. 4. Wake structure behind the hollow fly-swatter (left side) and fully covered fly-swatter (right side) for 20°, 40°, 60° and 80°. Transverse mean horizontal velocity $< v >$ (top row) and vertical velocity $< w >$ (second row), transverse velocity fluctuations v_{rms} (third row) and w_{rms} (bottom row).

The PIV measurements of the transverse components of the velocity field in the wake, 10 cm downstream of the center of the fly-swatter are shown in Fig. 4. For these measurements, the angle θ was set to four different constant values (namely 20°, 40°, 60° and 80°), with no free rotation allowed around point O, i.e. this is not a pendulum configuration. The Reynolds number for the PIV measurements is $\mathrm{Re} = 1.2 \times 10^4$. In each panel, the flow of the porous plate (the original fly-swatter) is displayed on the left half while the flow of the solid plate (fully covered fly-swatter) is shown on the right half. The two upper rows show the time-averaged structure of the wake, and the two lower rows the amplitude of the fluctuations. The PIV measurements are shown here with the purpose of illustrating the differences in flow features between the wake created by solid and porous plates, but no deep quantitative analysis is presented. We note strong differences between both configurations.

In the case of the solid plate, there is a clear difference below and above the stall angle ($\simeq 50°$). Strong trailing vortices (also known as wingtip vortices) with a large down-wash at the center are observed in the mean flow above the stall angle (*i.e.* 60° and 80°). While the down-wash is already present on the vertical component at 40°, no clear signature of the trailing vortices is visible on the horizontal component.

In contrast, the structure of the mean-flow is similar for all inclination angle for the porous plate; a feature shared with the fluctuating part. The maximal level of fluctuations of the solid plate is about three times that of the porous one. The influence of the stall angle for the solid plate is also evident, with very localized fluctuations are observed around the vortices above the stall angle.

B. Reducing the fraction of porous surface by concentric holes covering

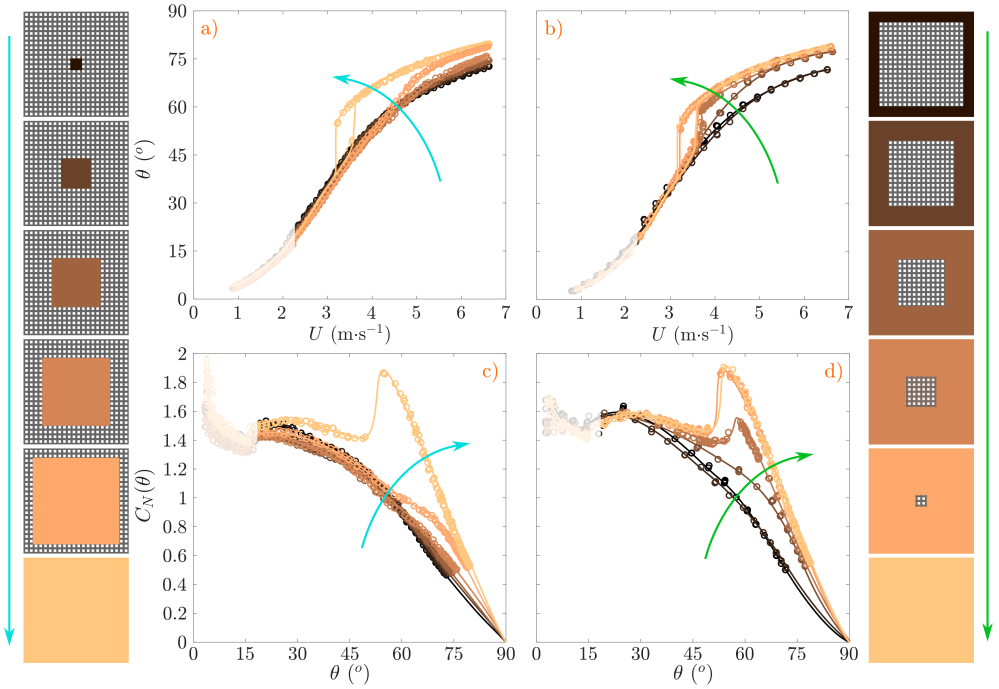

FIG. 5. Influence of concentric hole-covering. Top (a,b): evolution of θ as a function of U. Bottom (c,d): C_N coefficient computed from Eq. 1. Leftmost configurations (a,c): concentric covering from the center towards the edges. Rightmost configurations (b,d): concentric covering from the edges towards the center. Color codes for the configuration. The curves are spline interpolations and thus an eye guide.

The porosity pattern was first modified by concentric holes covering in two different ways: either from the center towards the edges or vice-versa. Six different configurations, for each concentric direction, are investigated, with five of them being partially porous and obtained by the addition of vinyl tape strips covering a two-hole wide band, as indicated in the side sketches of Fig. 5. When the fraction of porous surface is reduced from the center (left half in Fig. 5), no significant changes are observed on the evolution of θ with the velocity U, until covering the last two lines of holes on the edges. In particular, bistability is only observed for the fully taped configuration (see Fig. 5.a). This observation is in contrast with the behavior observed when the porous fraction is reduced when covering the holes from the edges towards the center (right half in Fig. 5). Bistable regimes are observed for several configurations, as soon as the central porous square is smaller than a 6×6-hole square (see Fig. 5.b). Almost no difference is observed between the solid case and the case when a 2×2-hole square is left open at the center. For bistable configurations, the evolution of the C_N coefficient with θ displays a sharp increase at the stall angle (see Fig. 5.c and d).

These results highlight the importance of the porosity of the edges for the existence of a sharp stall: the presence of holes on the edges of the plate prevent the occurrence of a sharp stall. On the contrary, stall can be readily observed in the presence of a significant porous fraction at the center of the plate.

As mentioned in the introduction, De Bray[31] presented similar concentric configurations of a

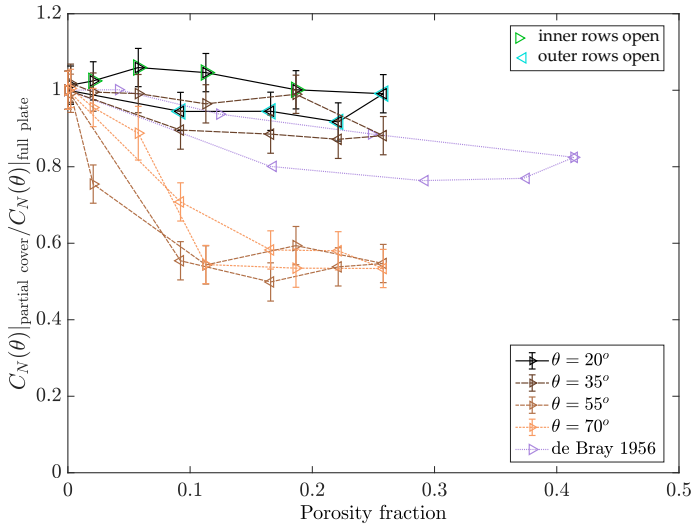

FIG. 6. Evolution of the normal coefficient C_N with the porosity fraction for $\theta = 20°$, $35°$, $55°$ and $70°$. The experimental data is compared with results at normal incidence ($\theta = 0°$) from De Bray[31].

porous plate at normal incidence $\theta = 0°$. Figure 6 displays the normal coefficient as a function of the porosity fraction (normalised by the normal coefficient for the full square), for various incidence angles from our experimental data, and those of De Bray at normal incidence. For low inclinations, $\theta = 20°$ and $\theta = 35°$, the normal coefficient is lower when the outer rows are uncovered than when the inner rows are uncovered, for similar values of the porosity fraction. These trends are similar to those of De Bray at normal incidence. On the contrary, for larger incidence angles, $\theta = 55°$ and $\theta = 70°$, the normal coefficient reduction with the porosity fraction is higher and both concentric hole-covering follow the same trend. These differences may be attributed to the fact that drag dominates for θ below $50°$, while lift dominates above.

C. Triggering stall from the edge porosity pattern

Section III B highlighted that bistability on the evolution of $\theta(U)$ and abrupt stall only appear when the last two lines of holes at the periphery of the plate are covered, when all the inner holes are covered. In order to better understand influence of edge porosity on the emergence of abrupt stall, seven configurations with a partially covered periphery were tested. Note that some of these configurations break the top-down symmetry, and that, following the convention of Fig. 3, the holding rod of the various configuration is placed at the top part of the sketches. Fig. 7 focuses on configurations for which the bistability is observed as the fraction of porous surface of the plate is decreased. Configurations, that, despite a similar porous fraction, present no bistability, are shown in Fig. 9.

The two leftmost configurations shown in Fig. 7 do not present any bistability, whereas bistability develops for the four rightmost configurations. When bistability is observed, the range of bistable positions increases with the covering fraction, *i.e.* from left to right. The bistability thus first arises, when in addition to the center of the fly-swatter, the top two rows are fully covered with tape. Covering the upper 4-holes corners on each side seems critical for the onset of bistability, since, when they remain uncovered (as in the second leftmost configuration), no bistability was observed.

The signature of bistable regimes is also readily observed on the evolution of $C_N(\theta)$ (see Fig. 7.b). A local increase of $C_N(\theta)$ is observed for angles between 50 and $70°$, seemingly correlated with the stall angle, that separates the lift and the drag branches. More precisely, we note that covering the two upper corners only induces a bump on the C_N coefficient between $57°$ and $65°$ (third leftmost configuration). This modest increase leads to an inflection point on the C_N coefficient, which is nonetheless sufficient to induce a sharp stall. As the porous fraction decreases further, the stall

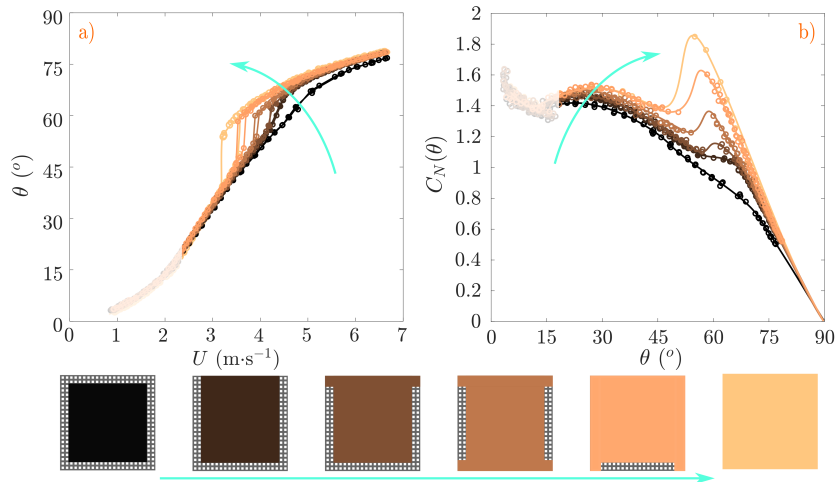

FIG. 7. Influence of outer rows hole-covering on bistability and sharp stall. Color codes for the configuration a) Evolution of θ as a function of U. b) C_N coefficient computed from Eq. 1. The curves are spline interpolations and thus an eye guide.

angle occurs for lower θ angles, decreasing from from 62° to 52°. The lift-dominated regime thus occurs over a larger range of angles θ (we recall that $\theta = \pi/2 - \alpha$, with α the angle of attack). Consequently, since bistability is observed around the stall angle, it occurs for angles that decrease as the porous fraction decreases. The range of velocity for which bistability occurs ΔU_{bistab} also decreases as the porous fraction increases as shown in Fig. 8 left axis, with a seemingly exponential decrease. Surprisingly though, the span of forbidden angles $\Delta\theta_{\text{forbidden}}$ (which are never explored neither in the lift branch nor in the drag branch) remains almost constant, around 5.5°, as shown in Fig. 8 right axis. Understanding whether this observation might be linked to the structure of the wake would require an extensive dataset of 3D flow measurements, out of reach of the present study.

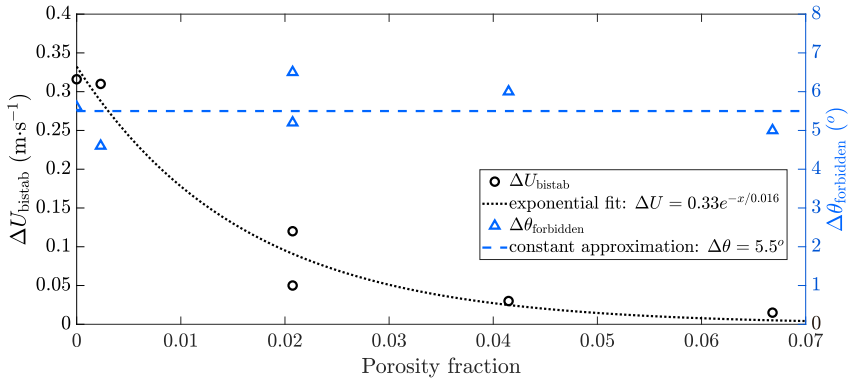

FIG. 8. Evolution of the bistable velocity range ΔU_{bistab} and forbidden angle span $\Delta\theta_{\text{forbidden}}$ as a function of the porous fraction.

No bistability, and thus no stall, was observed for any configuration shown in Fig. 9.a (apart from the solid plate). A specificity of all non-bistable configurations tested thus far is the presence of holes on the upper rows. For all these configuration, the evolution of the C_N coefficient with θ (see Fig. 9.b), does not display a strong bump in the range of angles $\theta \in [45°, 70°]$. We stress here that a weak bump is observed for the fifth leftmost configuration, around $\theta = 58°$, but which does not trigger bistable regimes. The values of the C_N coefficient observed for the solid plate on the drag branch ($\theta < 45°$) are recovered as soon as the lateral edges of the fly-swatter are covered.

This detailed study of the influence of the porous pattern at the edges of the plate suggests that

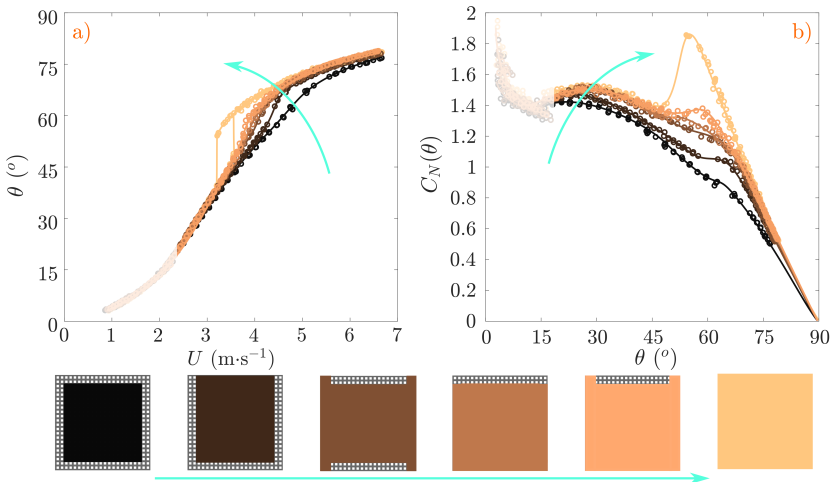

FIG. 9. Influence of outer rows hole-covering without bistability. a) Evolution of θ as a function of U. b) C_N coefficient computed from Eq. 1. Color codes for the configuration. The curves are spline interpolations and thus an eye guide.

a necessary condition for the existence of the bistability is the full covering of the upper rows. The configuration that displays bistability with the highest porous fraction is the third leftmost configuration shown in Fig. 7, with only the side and bottom edges left porous. On the other hand, the configuration with the least porosity that present no sharp stall is the second rightmost in Fig. 9, with only the leading-edge being partially hollowed.

Over the $2^{484}-19$ remaining configurations, *i.e.* more than 4.9×10^{145} configurations, we cannot rule out that these are not the ones with the respectively highest porous fraction for bistable regimes and lowest porous fraction for the absence of stall.

D. Curvature effects on C_N coefficient

Let us now briefly discuss a side effect of using a commercial fly-swatter as the initial porous plate: the effect of the weak natural curvature of the plate on its aerodynamic response. This effect was particularly experienced when testing whether the side covered by the tape influences the aerodynamics. The fly-swatter is indeed slightly curved and curvature can have a strong effect on aerodynamic properties, as observed already nearly a century ago by Flachsbart[42].

Four series of additional experiments were carried out for the concentric covering configurations, for which the face facing the incoming air flow could be either the concave or convex face, and could be the face covered or not by the adhesive tape. No influence of the side on which tape is glued was observed, while curvature orientation seems to greatly alter the aerodynamics, as shown in Fig. 10.

Let us first discuss the influence of curvature on the evolution of $\theta(U)$ for the six configurations shown in Fig. 10.a) and b). Several differences are noted : 1) the bistable zone is much narrower when the convex side faces upstream (b), 2) for the same flow velocity, for instance $U=6\,\mathrm{m\,s^{-1}}$, the angular position is lower when the convex side faces upstream.

These observations lead to large differences for the values of the C_N coefficient due to curvature (see Fig. 10.c and d). On average, for all configurations and all angles, the C_N coefficient is much higher when the concave side faces upstream. A striking observation is on the sharpness of the stall. For the fully-covered fly-swatter, the stall is indeed much smaller when the convex side faces upstream, with a factor of two for the amplitude of the discontinuity. The difference is also striking when the pendulum is close to the vertical position (*i.e.* for θ values below 18°), for which C_N appears to diverge when the concave side faces upstream (Fig. 10.c), while it decreases to 0 when the convex side faces upstream (Fig. 10.d). This feature is observed for all covering configurations,

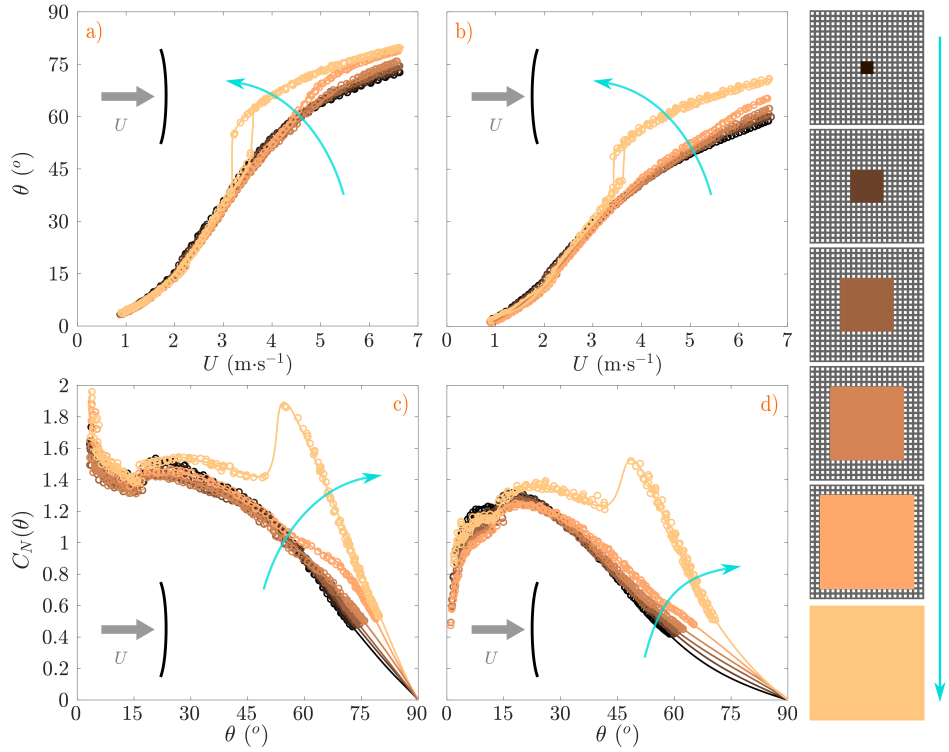

FIG. 10. Influence of curvature on the aerodynamic response of the partially covered fly-swatter. Top (a,b): evolution of θ as a function of U. Bottom (c,d): C_N coefficient computed from Eq. 1. Left (a,c): concave side facing upstream. Right (b,d): convex side facing upstream. Color codes for the configuration. The curves are spline interpolations and thus an eye guide.

which supports the conjecture that this is an effect of curvature.

All results presented in Sec. III A and III B and III D were obtained with the concave side facing the flow (*i.e.* the configuration of Fig. 10.a and c). Based on the observations for the concentric covering configurations, we expect to observe results similar to those reported in Sec. III C when the convex side faces the flow.

IV. CONCLUSION

By sealing holes on a fly-swatter, we were able to explore the influence of porosity patterning on the aerodynamic coefficients and bistability pendular porous plates. In spite of the simplicity of the considered system, several converging observations allow to draw some general conclusions regarding the role of certain porosity zones.

The existence of a sharp stall leads to bistable regimes as a function of the flow velocity in the pendular configuration, with bistability occurring around the stall angle. For a solid square plate, a sharp stall exists and the pendulum displays bistability.

No sharp stall has been observed for the other limit case, for which the square is homogeneously porous, leading to a continuous evolution of the pendulum angle with the flow velocity.

In all tested configurations that present a sharp stall the upper rows are indeed covered and a major part of the holes around the center are also sealed off. Seen in a different light, the bistability of a square plate disappears as soon as holes are opened in the upper rows (i.e. in the immediate vicinity of the leading edge), without impairing the lift production for angles $\theta > 70°$. Leading-edge porosity therefore appears as a possibly relevant strategy to dampen stall.

Surface porosity close to the leading-edge on airfoils has also been observed to reduce pressure load due to wing-vortex interactions[47]. PIV measurements of the evolution of the wake structure with the angle of attack for the two limit cases (solid and homogeneously porous square) clearly demonstrate that the observations made on the global aerodynamic coefficients are linked to the wake characteristics. A detailed study of the influence of the porosity pattern at the immediate vicinity of the leading edge on the wake structure and dynamics, and its relation with the existence of sharp stall was beyond the scope of the present work, but would represent a useful extension.

Another aspect not investigated here is noise reduction induced by the surface porosity. Indeed, porosity at the leading- and trailing-edge is often associated with noise reduction[48]. The small vortices induced by the pores destabilizes the large-scale leading- and trailing-edge vortices, which are responsible to a large extent for aircraft noise. This effect of porosity was, in fact, first observed in Nature[49] and biomimetic concerns spread it to aerospace engineering[50]. Owls are particularly known for their silent flight and recent studies have shown how the particular structure of their flight feathers enables this feat[51]. The owl feather presents serrations at its leading-edge, and sometimes also throughout the inner vane. Serrations are an ultra-thin comb of barbules and increase the porosity of the feather. The comb breaks the two-dimensionality of the leading-edge vortex which is no longer sustained[52]. Engineering aerodynamic noise generation by the fine tuning of the surface porosity of objects moving in a flow would also be a possible continuation of this work.

SUPPLEMENTARY MATERIAL

Supplementary material contains the data sets presented in Fig. 3, as a table file.

ACKNOWLEDGEMENTS

This work was partly supported by Initiative d'Excellence de Lyon (IDEXLYON) of the University of Lyon in the framework of the Programme Investissements d'Avenir (ANR-16- IDEX-0005) Université de Lyon. The authors would like to thank Samuel Bera for his involvement in the implementation of the PIV measurements. The authors thank the anonymous referees for raising points that helped clarify the manuscript.

REFERENCES

[1]P. Klebert, P. Lader, L. Gansel, and F. Oppedal, "Hydrodynamic interactions on net panel and aquaculture fish cages: A review," Ocean Engineering **58**, 260–274 (2013).
[2]E. M. Laws and J. L. Livesey, "Flow through screens," Annual Review of Fluid Mechanics **10**, 247–266 (1978).
[3]S.-J. Lee and H.-B. Kim, "Laboratory measurements of velocity and turbulence field behind porous fences," Journal of Wind Engineering and Industrial Aerodynamics **80**, 311–326 (1999).
[4]C. M. Regalado and A. Ritter, "The design of an optimal fog water collector: A theoretical analysis," Atmospheric Research **178-179**, 45–54 (2016).
[5]A. Moncuquet, A. Mitranescu, O. C. Marchand, S. Ramananarivo, and C. Duprat, "Collecting fog with vertical fibres: Combined laboratory and in-situ study," Atmospheric Research **277**, 106312 (2022).
[6]R. Mittal, R. Ni, and J.-H. Seo, "The flow physics of covid-19," Journal of Fluid Mechanics **894**, F2 (2020).
[7]L. Bourouiba, "The fluid dynamics of disease transmission," Annual Review of Fluid Mechanics **53**, 473–508 (2021).
[8]S. Aubrun, S. Loyer, P. Hancock, and P. Hayden, "Wind turbine wake properties: Comparison between a non-rotating simplified wind turbine model and a rotating model," Journal of Wind Engineering and Industrial Aerodynamics **120**, 1–8 (2013).
[9]M. Bastankhah and F. Porté-Agel, "A new analytical model for wind-turbine wakes," Renewable Energy **70**, 116–123 (2014).
[10]E. H. Camp and R. B. Cal, "Mean kinetic energy transport and event classification in a model wind turbine array versus an array of porous disks: Energy budget and octant analysis," Phys. Rev. Fluids **1**, 044404 (2016).

[11]N. Bempedelis and K. Steiros, "Analytical all-induction state model for wind turbine wakes," Phys. Rev. Fluids **7**, 034605 (2022).
[12]A. A. Ayati, K. Steiros, M. A. Miller, S. Duvvuri, and M. Hultmark, "A double-multiple streamtube model for vertical axis wind turbines of arbitrary rotor loading," Wind Energy Science **4**, 653–662 (2019).
[13]J. M. Jonkman and D. Matha, "Dynamics of offshore floating wind turbines: analysis of three concepts," Wind Energy **14**, 557–569 (2011), https://onlinelibrary.wiley.com/doi/pdf/10.1002/we.442.
[14]T. Messmer, M. Hölling, and J. Peinke, "Enhanced recovery and non-linear dynamics in the wake of a model floating offshore wind turbine submitted to side-to-side and fore-aft motion," (2023), arXiv:2305.12247 [physics.flu-dyn].
[15]S. Rockel, J. Peinke, M. HÃ¶lling, and R. B. Cal, "Wake to wake interaction of floating wind turbine models in free pitch motion: An eddy viscosity and mixing length approach," Renewable Energy **85**, 666–676 (2016).
[16]S. Rockel, J. Peinke, M. HÃ¶lling, and R. B. Cal, "Dynamic wake development of a floating wind turbine in free pitch motion subjected to turbulent inflow generated with an active grid," Renewable Energy **112**, 1–16 (2017).
[17]C. Cummins, M. Seale, A. Macente, D. Certini, E. Mastropaolo, I. M. Viola, and N. Nakayama, "A separated vortex ring underlies the flight of the dandelion," Nature **562**, 414–418 (2018).
[18]P. G. Ledda, L. Siconolfi, F. Viola, S. Camarri, and F. Gallaire, "Flow dynamics of a dandelion pappus: A linear stability approach," Phys. Rev. Fluids **4**, 071901(R) (2019).
[19]S. Sunada, H. Takashima, T. Hattori, K. Yasuda, and K. Kawachi, "Fluid-dynamic characteristics of a bristled wing," Journal of Experimental Biology **205**, 2737–2744 (2002).
[20]D. Kolomenskiy, S. Farisenkov, T. Engels, N. Lapina, P. Petrov, F. O. Lehmann, R. Onishi, H. Liu, and A. Polilov, "Aerodynamic performance of a bristled wing of a very small insect: Dynamically scaled model experiments and computational fluid dynamics simulations using a revolving wing model," Experiments in Fluids **61**, 1–13 (2020).
[21]G. I. Taylor, "Air resistance of a flat plate of very porous material," Tech. Rep. 2236 (Ministry of Supply, Aeronautical Research Council, London [England], 1944).
[22]G. I. Taylor and R. M. Davies, "The aerodynamics of porous sheets," Tech. Rep. 2237 (Ministry of Supply, Aeronautical Research Council, 1944).
[23]I. P. Castro, "Wake characteristics of two-dimensional perforated plates normal to an air-stream," Journal of Fluid Mechanics **46**, 599–609 (1971).
[24]J. M. R. Graham, "Turbulent flow past a porous plate," Journal of Fluid Mechanics **73**, 565–591 (1976).
[25]B. W. Robert, "Drag and pressure distribution on a family of porous, slotted disks," Journal of Aircraft **17**, 393–401 (1980).
[26]E. Villermaux and E. J. Hopfinger, "Periodically arranged co-flowing jets," Journal of Fluid Mechanics **263**, 63–92 (1994).
[27]K. Steiros, K. Kokmanian, N. Bempedelis, and M. Hultmark, "The effect of porosity on the drag of cylinders," Journal of Fluid Mechanics **901**, R2 (2020).
[28]J.-K. Koo and D. F. James, "Fluid flow around and through a screen," Journal of Fluid Mechanics **60**, 513–538 (1973).
[29]K. Steiros and M. Hultmark, "Drag on flat plates of arbitrary porosity," Journal of Fluid Mechanics **853**, R3 (2018).
[30]O. C. Marchand, S. Ramananarivo, C. Duprat, and C. Josserand, "Three-dimensional flow around and through a porous screen," (2023), arXiv:2303.00711.
[31]B. de Bray, "Low speed wind tunnel tests on perforated square flat plates normal to the airstream: Drag and velocity fluctuation measurements," Tech. Rep. 323 (A.R.C. technical report, 1956).
[32]L. Vincent, W. S. Shambaugh, and E. Kanso, "Holes stabilize freely falling coins," Journal of Fluid Mechanics **801**, 250–259 (2016).
[33]G. Vagnoli, G. Zampogna, S. Camarri, F. Gallaire, and P. Ledda, "Permeability sets the linear path instability of buoyancy-driven disks," Journal of Fluid Mechanics **955**, A29 (2023).
[34]R. R. Montgomery, "Fly killer," (1900).
[35]M. W. Gatch, "Fly swatter," (1927).
[36]P. J. Brownson, "Fly swatter," (1938).
[37]D. Baker, "Fly swatter," (1939).
[38]M. Obligado, M. Puy, and M. Bourgoin, "Bi-stability of a pendular disk in laminar and turbulent flows," Journal of Fluid Mechanics **728**, R2 (2013).
[39]A. Gayout, M. Bourgoin, and N. Plihon, "Rare event-triggered transitions in aerodynamic bifurcation," Phys. Rev. Lett. **126**, 104501 (2021).
[40]A. Gayout, A. Gylfason, N. Plihon, and M. Bourgoin, "Fluidelastic modeling of a weathercock stabilization in a uniform flow," Journal of Fluids and Structures **120**, 103895 (2023).
[41]X. Tian, M. C. Ong, J. Yang, and D. Myrhaug, "Large-eddy simulation of the flow normal to a flat plate including corner effects at a high reynolds number," Journal of Fluids and Structures **49**, 149–169 (2014).
[42]O. Flachsbart, "Messungen an ebenen und gewölbten Platten," in *Ergebnisse der Aerodynamischen Versuchsanstalt zu Göttingen - IV. Lieferung* (Verlag von R. Oldenburg, München und Berlin, 1932) pp. 96–100.
[43]S. Gao, L. Tao, X. Tian, and J. Yang, "Flow around an inclined circular disk," J. Fluid Mech. **851**, 687–714 (2018).
[44]J. Sommeria, "UVMAT," http://servforge.legi.grenoble-inp.fr/projects/soft-uvmat (2008).
[45]G. Eiffel, "Sur la résistance des plans rectangulaires frappés obliquement par le vent," Comptes-rendus hebdomadaires des séances de l'Académie des Sciences **151**, 979–981 (1910).
[46]M. Okamoto and A. Azuma, "Aerodynamic characteristics at low reynolds number for wings of various planforms," AIAA Journal **49**, 1135–1150 (2011).
[47]E. Eljack, I. AlQadi, and M. Khalid, "Numerical simulation of surface porosity in presence of wing-vortex interaction," Aircraft Engineering and Aerospace Technology **87**, 443–453 (2015).
[48]M. Zhang and T. P. Chong, "Experimental investigation of the impact of porous parameters on trailing-edge noise," Journal of Sound and Vibration **489**, 115694 (2020).
[49]R. R. Graham, "The Silent Flight of Owls," The Journal of the Royal Aeronautical Society **38**, 837–843 (1934).

[50]C. Rao, T. Ikeda, T. Nakata, and H. Liu, "Owl-inspired leading-edge serrations play a crucial role in aerodynamic force production and sound suppression," Bioinspiration & Biomimetics **12**, 046008 (2017).
[51]T. Ikeda, T. Ueda, T. Nakata, R. Noda, H. Tanaka, T. Fujii, and H. Liu, "Morphology Effects of Leading-edge Serrations on Aerodynamic Force Production: An Integrated Study Using PIV and Force Measurements," Journal of Bionic Engineering **15**, 661–672 (2018).
[52]C. Rao and H. Liu, "Aerodynamic robustness in owl-inspired leading-edge serrations: a computational wind-gust model," Bioinspiration & Biomimetics **13**, 056002 (2018).